Engineering surgical face masks with photothermal and photodynamic plasmonic nanostructures for enhancing filtration and on-demand pathogen eradication

Mohammad Ali Haghighat Bayan,[a] Chiara Rinoldi,[a] Daniel Rybak,[a] Seyed Shahrooz Zargarian,[a] Anna Zakrzewska,[a] Olga Cegielska,[b] Kaisa Põhako-Palu,[c] Shichao Zhang,[d] Agata Stobnicka-Kupiec,[e] Rafał L. Górny,[e] Paweł Nakielski,[a] Karin Kogermann,[c] Luciano De Sio,[f] Bin Ding,[d] and Filippo Pierini,[*a]

The shortage of face masks and the lack of antipathogenic functions has been significant since the recent pandemic's inception. Moreover, the disposal of an enormous number of contaminated face masks not only carries a significant environmental impact but also escalates the risk of cross-contamination. This study proposes a strategy to upgrade available surgical masks into antibacterial masks with enhanced particle and bacterial filtration. Plasmonic nanoparticles can provide photodynamic and photothermal functionalities for surgical masks. For this purpose, gold nanorods act as on-demand agents to eliminate pathogens on the surface of the masks upon near-infrared light irradiation. Additionally, the modified masks are furnished with polymer electrospun nanofibrous layers. These electrospun layers can enhance the particle and bacterial filtration efficiency, not at the cost of the pressure drop of the mask. Consequently, fabricating these prototype masks could be a practical approach to upgrading the available masks to alleviate the environmental toll of disposable face masks.

Introduction

In recent years, there has been an increasing focus on the health impacts of microbial components and particulate matter (PM), particularly since the onset of the COVID-19 pandemic.[1–3] When we breathe, cough, or sneeze, many respiratory secretions and saliva are released into the surrounding environment, creating infectious aerosols. These aerosols contain pathogenic particles that can deposit in living spaces and infect susceptible populations, leading to respiratory infections.[4,5] Numerous pathogenic bacteria and viruses have been shown to spread via aerosols, rapidly transmitting respiratory infectious diseases, particularly in enclosed spaces.[6] As a result, ensuring personal protection from infection is crucial and is a global issue.[7] Airborne PM is now recognized as one of the most harmful air pollutants significantly impacting air quality, public health, and ecosystems.[8,9] PM is classified as $PM_{0.3}$, PM_1, $PM_{2.5}$, and PM_{10} based on particle sizes smaller than 0.3, 1, 2.5, and 10 µm, respectively.[10] The most dangerous particles are those with aerodynamic diameters between 1.0 µm (PM_1) and 0.3 µm ($PM_{0.3}$), as they can travel long distances in the air and have a large surface area.[11,12] The mentioned features enable these particles to carry numerous pathogens and penetrate lung tissues and the blood-circulation system, resulting in respiratory and cardiovascular diseases. Face masks today are the potential means of protection from airborne pollutants emitted into the air.[13,14]

The primary issue with the available face masks is the short duration of functionality.[15] Personal protective equipment (PPE) has been severely in short supply during the COVID-19 coronavirus crisis, particularly concerning the accessibility of N95 and similar masks.[16] Many techniques have been explored for the quick and frequent disinfection of these masks and other PPE to address the difficulty of safely reusing face masks.[17–20] Over the past three years, gigantic mask consumption generated huge biomedical waste (BMW), mainly released into the environment without proper sterilization. Moreover, the massive production of BMW on a comprehensive level of society led to the merging of BMW with municipal solid waste.[18,21,22] Exposure of hazardous and contagious waste to municipal waste in the environment will be one of the most significant environmental issues. The urgent need to find a feasible solution for an antibacterial face mask has received less scientific study.[23,24]

One of the approaches is employing nanotechnology and nanomaterials to modify the available face masks. Electrospinning is a technique capable of fabricating fibers with the desired dimension and morphology.[25–28] This technique is widely used to manufacture fibers for filtration. Furthermore, stimuli-responsive nanomaterials have been fabricated via this technique for various applications.[29–31] Using this strategy to advance existing respirators/masks has been previously illustrated as a feasible roadmap,[32] introducing an adjustable layer with a desired porosity over the already-available face masks, which is scalable and achievable.

[a.] *Department of Biosystems and Soft Matter, Institute of Fundamental Technological Research, Polish Academy of Sciences, Warsaw 02-106, Poland*
[b.] *Laboratory of Polymers and Biomaterials, Institute of Fundamental Technological Research Polish Academy of Sciences, Warsaw 02-106, Poland*
[c.] *Institute of Pharmacy, Faculty of Medicine University of Tartu, Nooruse 1, 50411 Tartu, Estonia*
[d.] *Innovation Center for Textile Science and Technology, College of Textiles, Donghua University, Shanghai 201620, China*
[e.] *Laboratory of Biohazards, Department of Chemical, Aerosol and Biological Hazards, Central Institute for Labour Protection – National Research Institute, Warsaw 00-701, Poland*
[f.] *Department of Medico-Surgical Sciences and Biotechnologies, Research Center for Biophotonics, Sapienza University of Rome, Latina 04100, Italy*
† Footnotes relating to the title and/or authors should appear here.

Plasmonic nanoparticles can decorate the surface of fibrous materials for their physically driven antipathogenic activity.[17,33] This decoration enables an active pathway for reducing the accumulation of harmful and living pathogens in the pores of the fibers.[34] Such photothermally effective nanoparticles can induce light-triggered photothermal disinfection (on request) and have a broadband absorption range to eradicate any potentially lingering germs.[35–37]

Among plasmonic nanoparticles, gold nanoparticles (Au NPs) have been widely used in numerous scientific domains in recent years due to their optical and thermo-optical features.[31,38–40] Localized surface plasmon resonance (LSPR), a physical phenomenon, enables Au NPs to produce a strong electromagnetic field at the nanoscale level.[41] The coherent and dipolar oscillation of free electrons localized at the metal/dielectric interface is related to LSPR.[42-43] The LSPR oscillation produces a significant temperature increase on the surface of the Au NP when it is exposed to an appropriate (resonant) light source, converting the Au NP into a focused nano source of heat.[44,45] It was abundantly evident that influential LSPR absorption, followed by quick energy conversion and dissipation, could efficiently heat the immediate environment and kill microorganisms.[46,47]

Researchers have studied and reported air filters and masks endowed with photo-responsive properties.[48-51] Li et al. investigated the potential of metal-organic frameworks (MOFs) for air pollution control and personal protection, focusing on a zinc-imidazolate MOF with photocatalytic bactericidal properties.[48] The fabricated MOF-based air filters not only achieve efficient particulate matter removal but also demonstrate remarkable photocatalytic antibacterial behavior. In another research, Kumar and coworkers presented the development of modified polycotton fabrics with molybdenum disulfide (MoS_2) nanosheets.[49] The modified fabric offered self-disinfection, antibacterial, and photothermal properties for reusable protective masks. The study highlighted the potential for cost-effective, large-scale production of nanosheet-modified antibacterial fabrics. Shao et al. explored the antibacterial properties of gold nanomaterials, including gold nanospheres (Au NSs) and gold nanorods (Au NRs), as well as silver nanoparticles (Ag NPs) under incandescent light exposure.[51] The results reveal that Au NSs do not exhibit significant antibacterial activity, while Au NRs demonstrate substantial bactericidal effects against various bacterial strains. This antibacterial effect is enhanced by the photodynamic and photothermal properties of Au NRs when exposed to NIR light, leading to bacterial inactivation. These findings highlight the potential of AuNRs in photoactivated bacterial inactivation.

We developed and optimized a strategy to introduce homogenous defect-less electrospun sandwich-like layers. This architecture will be a good candidate for indoor bactericidal eradication upon NIR light. The structured layers stayed on the outer layer of the surgical face mask. The introduced layer was then decorated with Au NRs. The nanorods have encapsulated between layers of electrospun nanofiber to avoid their leakage. These nanofibrous layers can capture fine particles and maintain the applicability and performance of commercial surgical face masks. The decorated nanofibers introduced an on-demand antibacterial feature that can activate under the face masks' near-infrared region (NIR) light irradiation. The design of the face mask is intended for bacterial elimination after each wearing through the NIR irradiation process. The antibacterial activity and electrospun layer simultaneously can improve the face mask's bacterial and PM filtration efficiency. This innovative platform is designed to eliminate surface bacteria on face masks effectively. This key feature not only answers the needs of the general public but also holds particular significance for those in contact with hospital patients, helping prevent cross-contamination and the spread of diseases. Correspondingly, this prototype mask can prevent cross-contamination and the spread of infection and increase the functionality of the available surgical masks.

Results and discussion

Development and structural features of the platform

A feasible modification would extend their duration of functionality, aimed at designing new functionalities for commonly used masks. Therefore, the first step of fabricating the prototype face mask was to electrospun the first layer of polymer nanofibers on the surgical mask. An optimized electrospun polyacrylonitrile (PAN) layer was deposited on the surgical mask's outer layer. Afterward, the Au NRs alcosol suspension was electrosprayed on the surface of the PAN nanofibers. To make a protective layer for the electrosprayed nanoparticles on the as-decorated PAN electrospun nanofibers, an additional layer of pristine PAN nanofibers covered the Au NRs-PAN electrospun layer. Au NRs in this platform provide stimuli-responsiveness for the fabricated masks upon NIR light. The selected Au NRs for this study have the maximum absorption peak at 810 nm, which is the NIR region of the electromagnetic spectrum.[52,53] The gold nanoparticles triggered by NIR light excite their free electron from the plain state of S_0 to the excited S_1 electronic states.[54] After this excitation, gold nanoparticles, to come back to the equilibrium state, will release thermal energy at the nanoscale. In the developed platform, taking advantage of generated heat can lead to an on-demand feature for eliminating the potential bacteria on the surface of the face mask. Fig. 1 illustrates material preparation and the schematic response of gold nanoparticles. Regarding the general performance of face masks, surgical masks have low $PM_{0.3}$ and bacterial filtration efficiency (discussed further below). However, they are not capable of antibacterial activities. While the proposed modification of face masks illustrated a significant improvement in bacterial and particle filtration efficiency, they are equipped with on-demand antibacterial properties.

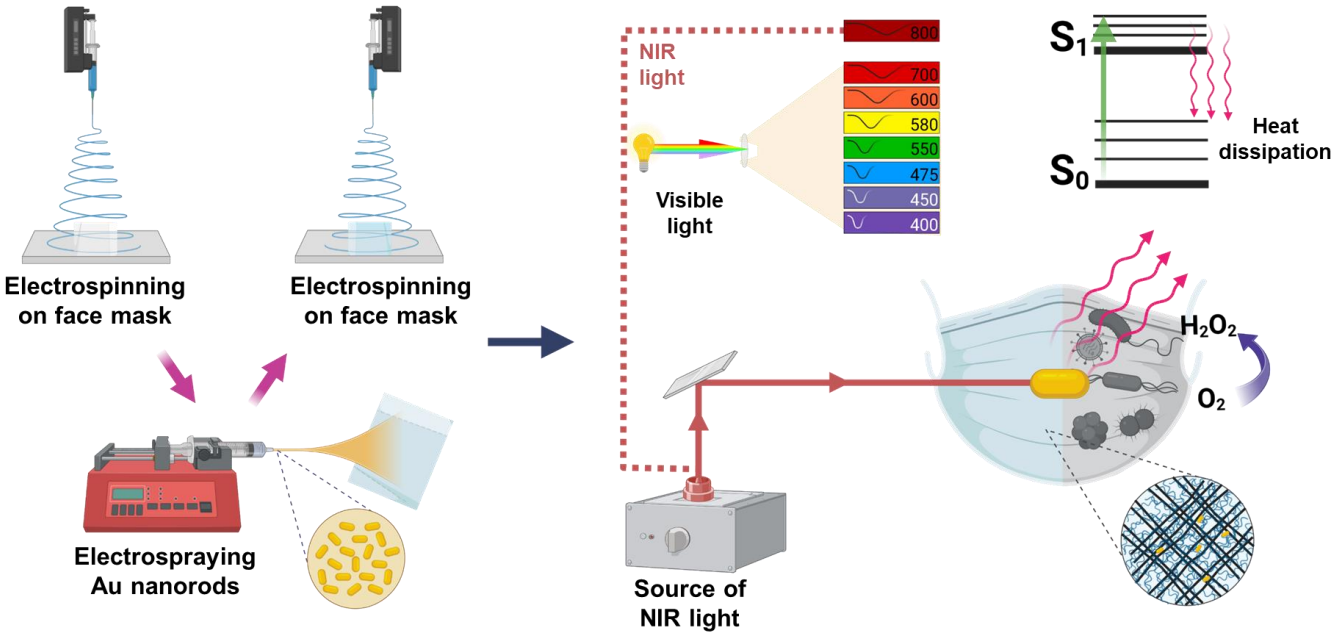

Fig. 1 Stratagem of modified face mask and novel features given by electrospinning and electrospraying. The schematic illustration shows the concept and structure design of the photo-response and photo-dynamic face mask fabrication. PAN nanofibers are formed firstly by electrospinning on a surgical mask, followed by Au NRs electrospraying procedure, and finally, PAN electrospun again on the decorated mask to create a protective layer for the nanoparticles. The nanostructured platform can efficiently be activated under the NIR irradiation.

Characterization and Properties of Gold Nanorods

Au NRs were introduced onto the nanofiber-layered masks to equip them with antibacterial properties enabling photo response-ability. The transmission electron microscope (TEM) image of the Au NRs used for this study can be seen in Fig. 2a. Two Au NRs are presented in the TEM micrograph. In Fig. S1, the TEM image displayed that the average length of nanorods is 50.8 ± 5 nm. Moreover, the TEM image analysis revealed that the gold nanorods' average width is 12.1 ± 0.8 nm with an average aspect ratio of 4.2 ± 0.6. The elemental mapping under a TEM (Fig. 2b) confirmed the presence of gold nanorods. As shown in Fig. 2c, Au NRs displayed strong absorbance in the NIR light region (810 nm). This absorbance is related to the length and aspect ratio of the Au NRs. The dynamic light scattering (DLS) curve of Au NRs in Fig. 2d shows an average hydrodynamic diameter of 50 nm, confirming the morphology of the gold nanoparticles used for this research.

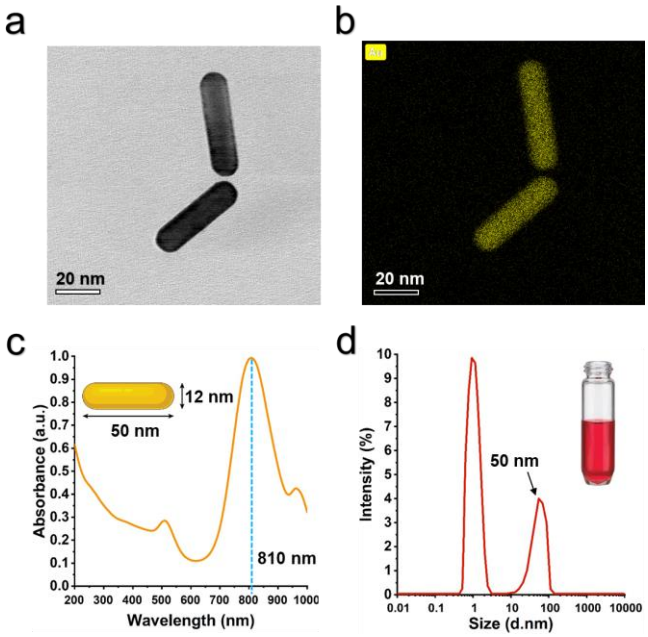

Fig. 2 Characterization of Au NRs utilized for this study. a) High-resolution TEM image of two gold nanoparticles. b) EDX elemental mapping image confirming the presence of gold. c) UV-Vis spectrum of Au NR solution exhibiting the sharp absorbance peak at 810 nm related to the morphology and aspect ratio of the employed nanorods. d) DLS plot presenting the hydrodynamic radius of nanorods approximately at 50 nm and an additional peak centered at 1 nm related to the nanorod rotational diffusion.

Face mask modification procedure

To prepare the electrospinning solution, first, PAN was dissolved and transferred to a syringe to fabricate an electrospun layer over the outer layer of the surgical face mask. The next step was to decorate the as-spun PAN layer. Due to the high hydrophobicity of polypropylene (PP) melt-blown fibers and PAN electrospun layer (Fig. S2), depositing uniform Au NRs was impossible. Soliwoda et al. proposed using alcosol of Au NRs instead of an aqueous solution to overcome this matter.[55] Subsequently, after the preparation of Au NRs alcosol, the as-spun PAN layer was decorated with Au NRs by electrospraying technique to equip the mask with photodynamic and photothermal properties. Finally, we employed electrospinning of PAN on the decorated layer to fabricate a protective layer for the decorated fibers. The described strategy allows the nanoparticles to be incorporated onto the electrospun layer and maintain their functionality without leaching. The binding forces between citrate-capped gold nanoparticles primarily involve electrostatic forces and coordination bonds. Citrate ions

(from citrate molecules) are commonly used to stabilize and cap Au NPs. Additionally, citrate molecules can form coordination bonds with gold atoms on the nanoparticle surface. This contributes to the stability of the citrate-capped Au NPs.[56] Furthermore, due to the robust entrapment of the nanoparticles within the layers, the chance of escape or inhalation of gold nanoparticles is minutest. Consequently, the functionality of Au NRs is retained, and they can effectively exhibit photodynamic and photothermal activities without creating potential health risks. In Fig. 3a, the process of preparing antibacterial face masks is illustrated. The available surgical face masks mainly consist of three melt-blown layers of PP. As the structure of surgical masks has been shown in Fig. S3a, the SEM micrographs show that the thickness of the internal and external layers are approximately 334 ± 23 µm and the thickness of the mid-layer is approximately 233 ± 16 µm (Fig. S3b). Additionally, the PP melt-blown fibers used for commercial face masks have an average diameter of 18 ± 0.83 µm, as is shown in Fig. 3b. The morphology of the fabricated PAN electrospun nanofibers has been shown in Fig. 3c. The electrospun fibers of PAN are beadless, uniform, and have an average diameter of 387 ± 49 nm. Fig. 3d shows the SEM micrograph of the surgical mask's PP fibers covered with PAN nanofibers. Herein, the comparison of surgical mask microfibers with the PAN nanofibers is visible and illustrates a significant increase in the potential of PM filtration (Fig. 3d). The electrospinning of PAN over the face mask provided a physical entanglement between the melt blown and nanofibers. The SEM image of the entanglement can be seen in Fig. 3e. In Fig. 3f, the SEM image of the cross-section of the prototype face mask showing the thickness of the delicate and efficient electrospun layer of PAN is about 8.45 µm can be seen. The FE-SEM image of Au NRs decorated nanofibers is presented in Fig. 3g, indicating the presence of Au NRs with an average length of 50 nm on the surface of electrospun PAN fibers is visible in this panel. SEM micrographs and the connected EDAX gold elemental mapping collected from three different representative areas of decorated face masks can be seen in Fig. S4. The central area and two other zones localized in the face mask's corners are visualized to appreciate the homogeneous distribution along the electrosprayed samples' area.

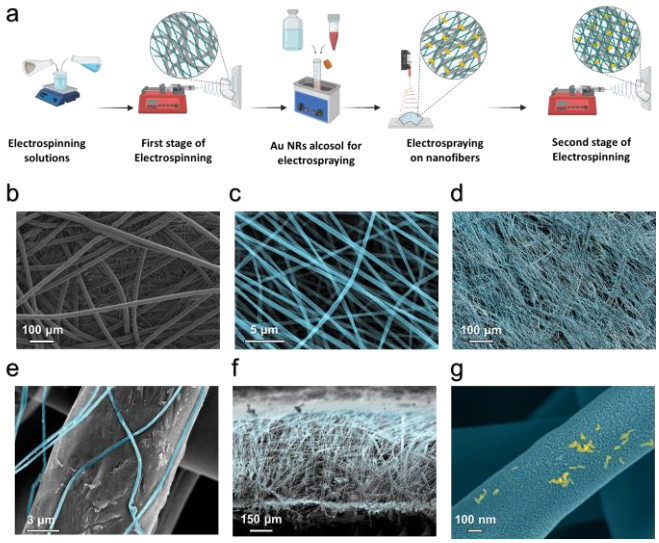

Fig. 3 Procedure of fabrication of nanostructured layer and morphological characterizations of the surgical mask (gray), PAN electrospun nanofibers (blue), and gold nanoparticles (yellow) fabricated for this study. a) The nanostructured face mask fabrication scheme consisted of two electrospinning steps and one electrospraying stage. b) SEM image of PP melt-blown surgical mask fibers. c) SEM micrograph of standalone PAN nanofibers. d) FE-SEM image of deposited PAN nanofibers on the outer layer of the face mask. e) SEM image showing anchorage of a PAN electrospun nanofiber on the surface of PP melt-blown fiber. f) Cross-section microscopic image of fabricated nanostructured face mask. g) FE- SEM image of PAN nanofibers decorated with Au NRs.

Photo-responsiveness of the fabricated masks

The photothermal property of modified masks was evaluated under laser irradiation. A NIR laser source operating at 810 nm wavelength was irradiated on the samples passing through a custom-designed optical path to investigate the photo-responsiveness of the fabricated face masks. The schematic of photo-response studies is illustrated in Fig. 4a. Any temperature change of the samples during irradiation was recorded and saved on the computer using a thermal camera. To observe the effect of NIR light on a surgical mask, plots of the temperature-time of untreated face masks under different powers of NIR light are reported in Fig. S5a. The NIR light with 0.5 W/cm^2 power increased the temperature of the outer layer of the face mask by 1 °C in 5 min of irradiation. Moreover, 3.0 W/cm^2 and 4.0 W/cm^2 NIR lasers were able to raise in temperature of the surgical mask respectively by 7.2 °C and 10.6 °C. Decorated face masks were irradiated by laser for 5 min with different NIR powers (Fig. S5b) to find the optimum laser power for the self-sterilizing mask. Applying a 0.5 W/cm^2 laser was able to reach 41.5 °C on the surface of the face mask. On the other hand, a 4.0 W/cm^2 NIR light could increase the temperature to 115.0 °C. At the same time, a 3.0 W/cm^2 laser was the optimum power, which raised the temperature to 113.2 °C, which can eradicate the pathogens via photothermal and photodynamic effects.[57,58] The temporal plots of decorated face masks were graphed (Fig. 4b) to optimize the concentration of Au NRs alcosol and find the proper duration for electrospraying. The material was designed to reach sufficient temperature to eradicate the bacteria for the dry and wet face masks (Fig. 4c). To mimic the operative conditions of the surgical face mask, i.e., accounting for the moisture that resides in the human exhale, the fabricated face mask can increase the temperature in a semi-wet scenario. The line profile plot module of the outer layer of the face mask shows a temperature of 113.5 °C along the surface of the mask (Fig. 4d). Furthermore, due to the application of decorated masks as wearable photoresponsive face masks, in Fig. 4e and f, the effect of laser irradiation on both sides of the platform has been studied. Meanwhile, the temperature of the inner layer, which is in contact with the user's skin, is about 29.5 °C showing the usability and safety of the fabricated platform. Fig. 4g is the thermographic image of decorated face masks under a 3.0 W/cm^2 NIR laser. Images captured by the thermal camera showed a rapid rise in platform temperature, regarded as the direct responsiveness rate. In Fig. S6, the thermographic image

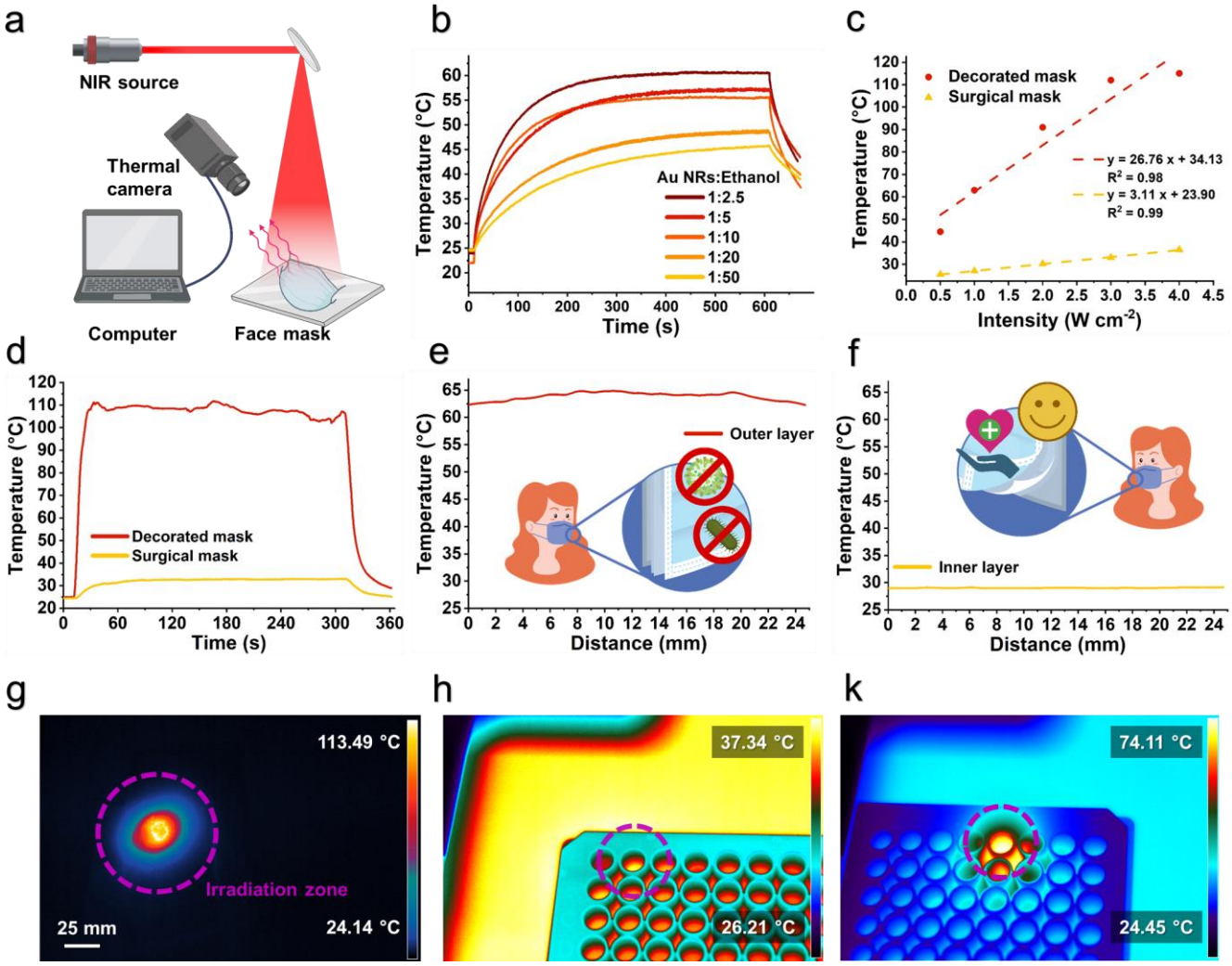

Fig. 4 The fabricated nanostructured face mask's photothermal representing the fabricated platform's fast responsiveness. a) Scheme displaying the experimental setup designed to analyze the photo-response of the modified face mask under NIR irradiation. The temperature change was recorded during the analysis using a thermal camera. b) Temporal plot of face masks decorated with different concentrations of Au NRs. The legends represent the volume ratio of the Au NRs solutions to ethanol in electrosprayed alcosol. Each sample was electrosprayed for 20 minutes. c) Linear correlation between the maximum temperature sensed by the thermal camera and the intensity of the NIR-laser for dry surgical and decorated face masks. d) Temperature vs. time plots of the nanostructured face mask decorated with Au NRs and untreated surgical mask under NIR-light irradiation for 5 min. e) Temperature distribution graphs of the outer layer of the nanostructured face mask. f) Temperature distribution graphs of the inner layer of the irradiated mask showing the temperature of 29.5 °C and safe for the user's skin. g) Thermograph image of the nanostructure face mask under NIR light irradiation (intensity of 3.0 W/cm2) showing a maximum temperature of 113.5 °C. h) Thermal image of circular cut surgical mask treated with bacteria suspension showing the temperature of the sample and hot plate for the study was steady around 37 °C. k) Thermogram of the nanostructured face mask cultured with bacteria under NIR-laser, in which the temperature reached 74 °C.

of a non-decorated face mask is visible. This figure indicates that the maximum reached temperature of a surgical mask under laser irradiation can be 32.56 °C which is not enough to eradicate pathogens.[36] To prepare and investigate specimens we utilized later for antibacterial studies (to be discussed whereafter), face masks were cut in circles and fixed at the bottom of 96-well plates. Fig. 4h and 4k show the thermographic images of the cut face masks during the antibacterial studies inside well plates. For this study, a hot plate was used to maintain the temperature of the samples at 37.0 °C imitating the wearer's face temperature. In Fig. 4h, the thermographic images of face masks during the antibacterial studies show that the temperature of the surgical mask was steady at 37.3 °C under NIR light irradiation. Meanwhile, in Fig. 4k, the decorated face mask displayed a rise in temperature to 74.1 °C under NIR irradiation for 15 min, which can be associated with the photothermal feature of Au NRs.

ROS generation of plasmonic nanoparticles

Recent research has focused on developing new and innovative methods for killing bacteria. One such method involves generating reactive oxygen species (ROS) generation with Au NRs. Gold nanorods can be utilized to generate ROS when irradiated with light. These generated ROS can damage bacterial cell walls and membranes, ultimately leading to cell death.[59,60] This approach has the potential to be highly effective in eliminating bacteria. The reactivity of Au NRs and their potential to generate ROS was determined in PBS over time.[61–63]

Deacetylation and purification of $DCFH_2$ in the present study were performed from an aqueous NaOH solution and purified by liquid phase extraction. The schematic of the preparation and purification steps is shown in Fig. 5a illustrating the different steps to prepare the $DCFH_2$ solution. Remarkably, during and after the preparation of $DCFH_2$, the solution was shielded from light to avoid oxidation upon light exposure. The absorption spectrum of $DCFH_2$ dissolved in methanol is shown in Fig. S7. The spectrum has an absorption maximum at λ = 231 nm. The spectrum of dissolved $DCFH_2$ shows the identification of organic functional groups.[64] The scheme in Fig. 5b shows the ROS generation upon NIR-light irradiation via Au NRs. A significant increase in DCF fluorescence occurred after the NIR laser irradiation of the Au NRs decorated face mask sample (Fig. 5c) in both decorated samples. In contrast, the fluorescence increase in the mentioned sample without laser irradiation was marginal, the same for the face mask without Au NRs. Similarly, DSC fluorescence of the surgical mask did not have a tangible change upon laser irradiation.

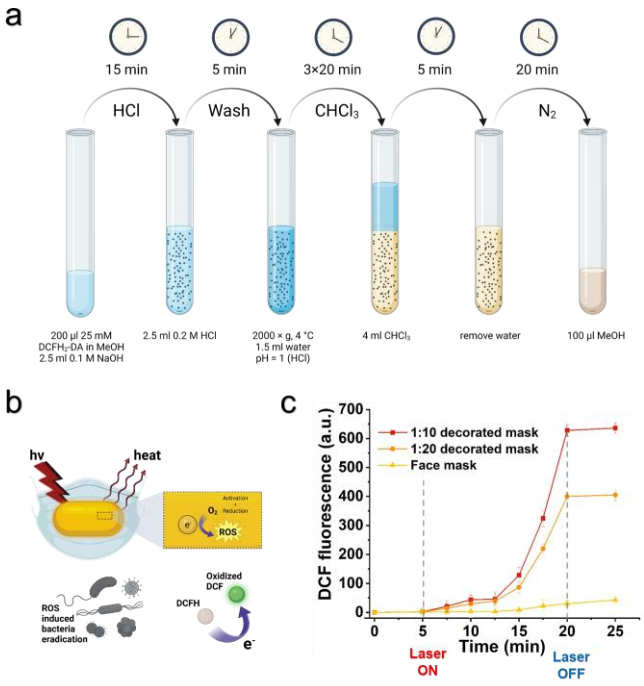

Fig. 5 ROS generation ability of Au NRs decorated face masks a) Standard procedure for the preparation and purification of DCHF2 b) Schematic of ROS generation upon NIR-light triggered via Au NRs. c) DCF fluorescence of different samples. Face mask decorated with two different concentrations of Au NRs and surgical face mask fluorescence changes over time.

Biocompatibility of the face masks

Different approaches were used in this study to evaluate the breath safety of the fabricated face masks. According to the ISO guidelines (109993-5), cell cytotoxicity was measured by indirect and direct methods to follow the cells' viability, proliferation, and morphology changes on or in close contact with the mask.[65] The schematic of the direct and indirect cell viability methods can be seen in Fig. 6a. In the case of the indirect method for evaluating cell viability, cells were seeded onto the well plate, and their growth medium was replaced with the medium where the mask samples were soaked for 24 h. The indirect method results showed that the nanostructured masks did not leach any cytotoxic substances (or did not reach high enough concentrations of substances) into the aqueous medium during the experiment and therefore had no toxic effect on cells. In Fig. 6b, no statistical difference in cell viability was found between the nanostructured face masks tested (single and double electrospun layer on the surgical mask) and traditional surgical face masks. The results of the direct cell viability evaluation can be seen in Fig. 6c. Similar to the indirect cell viability method, there were no statistically significant differences between tested masks and the controls at different time points, indicating the safety of tested masks.

In addition to the MTS direct cell viability assay, confocal microscopy was used to evaluate the safety and direct effect of nanostructured material of surgical mask on cell viability and proliferation. Fig. 6d shows confocal microscopy images of cells grown on tested masks for 48 h. No morphological changes in cells were observed when tested masks were compared to the control sample (cells cultured on round microscopy glass). It is possible to see even cell divisions, and the latter also indicates the well-being of the cells on top of the developed masks. Live cell staining and microscopy analyses were performed (Supportive information, Fig. S8) to confirm that the fixation process during the sample preparation for imaging did not affect the cells on masks. Similarly, no morphological changes of the BHK-21 cells were observed when these cells were grown on the masks containing fibers and Au NRs on top compared to the surgical mask.

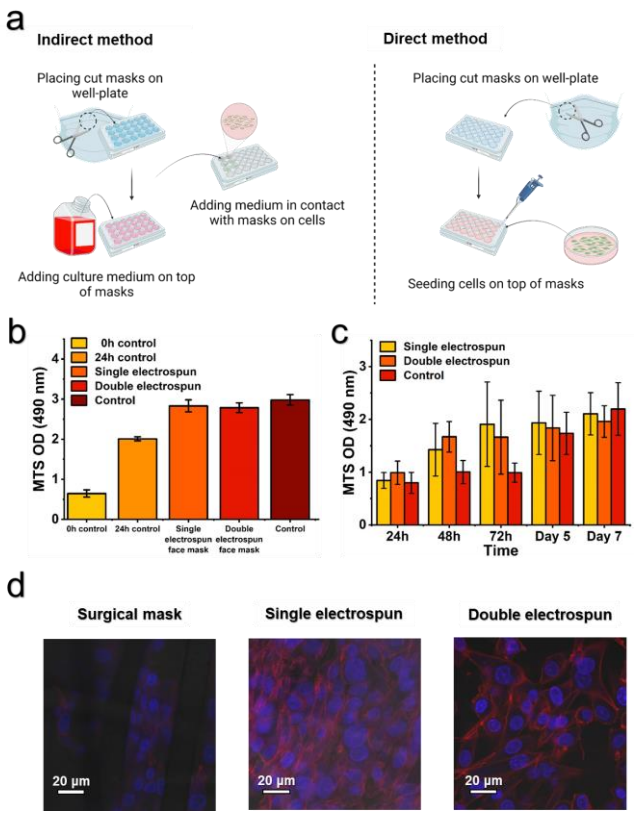

Fig. 6 Cell viability evaluation of BHK-21 exposed to different face mask samples. a) Schematic illustrating the steps for indirect and direct methods. b) indirect cell viability assay results, showing no statistically significant difference between analyzed face masks and the control sample after 48 h. The control sample is cells on the well plate. c) Results of direct cell viability method. Untreated cells grown at the bottom of the 24-wallplate were a control sample. d) Confocal microscope images of BHK-21 cells on face mask samples. The blue color in the microscopic images stands for the nucleus, which was stained with DAPI, while red actin filaments stained are with Phallodine conjugated Alexa 568.

Bacteria and particle filtration performance

Bacterial filtration efficiency (BFE) and particle filtration efficiency (PFE) are test methods to evaluate face masks, respirators, and filtration media performance efficiency.[66,67] Fig. 7a shows the schematic of BFE and PFE tests and the fabricated face mask structure. BFE and PFE tests were conducted to evaluate the functionality of the face masks. Moreover, the results of these tests could be beneficial to optimize the thickness of the fabricated electrospun layers. The BFE testing method was assessed following the EN 14683:2019+AC standard. In Tables S1-3, the total number of *Staphylococcus aureus* (*S. aureus*) bacteria that permeate the masks and their BFEs calculated following the mentioned standard can be found. To evaluate the effect of electrospinning, surgical mask, and electrospun face masks with single and double electrospun layers were analyzed. As can be seen in Fig. 7b, the BFEs were calculated as 55.24% ± 2.64, 90.16% ± 2.93, and 92.22% ± 3.53 for the surgical mask, single electrospun layer, and double electrospun layer, respectively. The results indicate that applying a layer of nanofibers to surgical face masks results in a statistically significant increase in the bacterial filtration efficiency of available surgical face masks. Additionally, to further investigate the effect of electrospun modification on the surgical mask, a PFE test was conducted with PM0.3-like NaCl particles. As shown in Fig. 7c, the measured PFE of surgical face mask is about 37% ± 1.04, while the filtration efficiency of single and double electrospun layer masks are 67% ± 5.14 and 71% ± 5.62, respectively. The PFE test exhibited that the modified electrospun face mask can enhance the $PM_{0.3}$ filtration twofold with a double electrospun layer structure. Finally, Fig. 7d shows the pressure drop of the surgical and electrospun-modified face masks. The double electrospun layer face mask exhibited high BFE efficiency and escalated the $PM_{0.3}$ filtration while maintaining a similar pressure drop. In addition, the double-layer electrospun face mask pressure drop was 30.3 Pa, while the pressure drop of the surgical face mask was 25.1 Pa revealing the superior performance of fabricated face masks.

Bacteria eradication of the face mask

Photothermal and photodynamic bacterial inactivation properties of the materials are performed upon NIR laser irradiation. The antibacterial tests were evaluated using bacterial suspensions of *S. aureus.* This species was selected since it is one of the most common microorganisms, and it is responsible for a wide range of clinical infections.[68]
Antibacterial analysis was performed to evaluate the antibacterial properties of fabricated face masks. The test

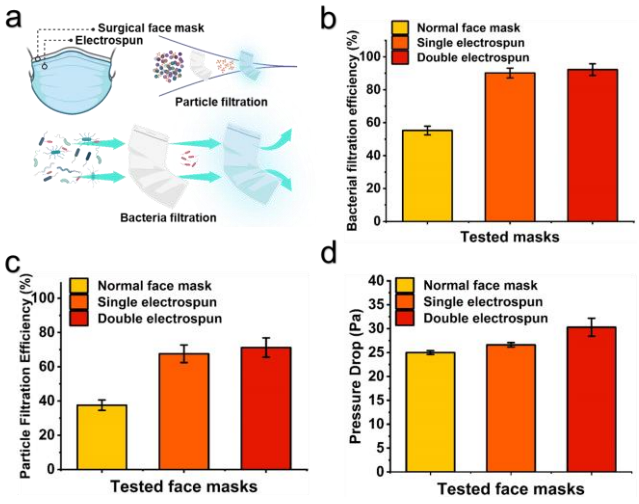

Fig. 7 a) Schematic of BFE and PFE tests. b) BFE of surgical masks compared with fabricated nanostructured platforms, showing enhancement in bacterial filtration. c) PFE performance of surgical masks, single and double electrospun layer face masks, presenting a considerable improvement in particle filtration efficiency. d) Pressure drop of fabricated single and double electrospun layer compared with surgical face mask showing maintain in pressure drop.

schematic is reported in Fig. 8a. The photothermal effect of Au NRs on bacteria suspension was observed after approximately 15 min of irradiation (Fig. 8b). During this time, in the presence of the Au NRs-coated masks, *S. aureus* was inactivated to the detection limit of 3 log units, demonstrating bacterial survival below 0.1% (Fig. 8c). No colonies were also observed in the representative plates, demonstrating effective inactivation of

99.95% of bacteria in the suspension, thus proving the self-sterilizing properties of the face masks under NIR-light-radiation conditions. By contrast, no bacterial inactivation was observed for Au NRs-free masks upon illumination and for any tested samples without irradiation. Additionally, no effect of irradiation on control bacterial suspension was detected.

The bactericidal performance of the Au NRs-coated masks towards *S. aureus* was caused by the synergistic effect of the hydrophobicity of the masks and the photothermal performance of Au NRs, as reported in Fig. 4k. Various shapes of Au nanoparticles belong to a group of photosensitizers, which generate excited triplet states when exposed to light. These interact with molecular oxygen and create singlet oxygen, damaging cell walls, plasma membranes, and DNA and eventually leading to the death of the microbial cells.[69-70] As the irradiation provided by the source of NIR light is continuous or recurring, the pathogens remaining on the surface of Au NRs-coated facemasks can be easily eliminated in a repeated manner. Besides, the exposure time and temperature achieved during the experiments were also reported as sufficient to accomplish 4 log decays of SARS-CoV-2.[71]

The effect of Au NRs to eliminate the bacteria on the surface of fabricated face masks was further visualized using electron microscopy. For this purpose, two representatives decorated face masks with Au NRs cultured with *S. aureus* bacteria were examined. The first face mask was cultured with bacteria but was not irradiated by NIR light. The non-irradiated face mask did not show antibacterial activities. The colonies of *S. aureus* are visible in the image and marked with yellow arrows (Fig. 8d). On the other hand, the on-demand antibacterial effect of NIR irradiated Au NRs decorated face masks is visible on the micrographs (Fig. 8e) showing the elimination of the bacteria on the face mask.

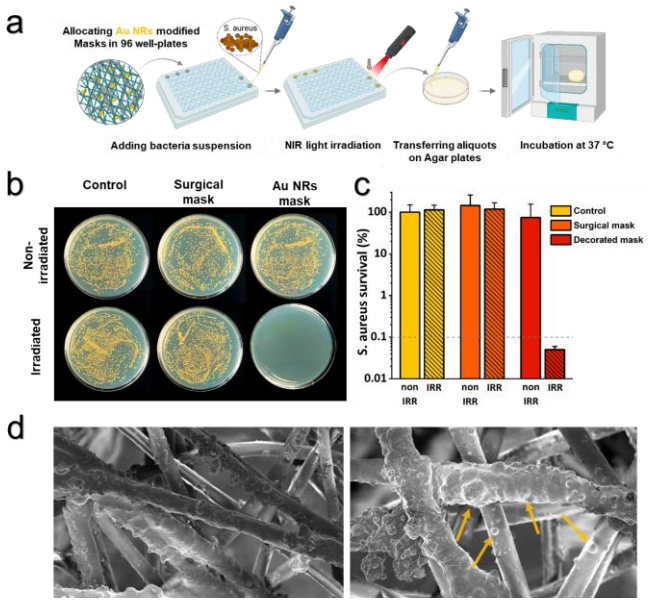

Fig. 8 Photothermal and photodynamic inactivation of S. aureus on Au NR-masks. a) Schematic representation of the antibacterial test procedure. b) Macroscopic pictures of bacterial colonies grown on LB agar c) Percent of bacteria survival after contact with bacterial suspension (control), mask, and Au NR-coated mask under NIR irradiation (IR) or dark incubation (n=3). The detection limit at 103 CFU/mL is marked with the dashed line. Data points below the detection limit are set as 0.05% bacteria survival. Data are reported on a logarithmic scale as mean ± standard deviation. d) SEM micrographs of face mask fibers cultured with bacteria; bacteria are marked with yellow arrows. e) SEM images of fabricated face mask after NIR irradiation showing the elimination of bacteria on the surface of the mask

Conclusions

This study displays a strategy to fabricate face masks with on-demand pathogen eradication capability. The strategy illustrated a way to decrease the environmental impact of many contaminated waste masks and the risk of spreading infections. The face mask's active layer consists of PAN electrospun nanofibers sandwiching Au NRs. The plasmonic nanoparticles electrospraying process offered the platform a combination of photothermal and photodynamic features. The antibacterial property of the platform is activated upon exposure to the NIR light and can eliminate 99.95% of bacteria on the surface of the face masks. Furthermore, the electrospinning technique improved nearly twice the face masks' particle and bacterial filtration efficiency. The study proved that obtaining a self-sterilizing face mask with boosted filtration properties has the potential for practical application. This developed structure will be a breakthrough for the face pieces industry for indoor bactericidal eradication applications as for hospital purposes. We engineered the face mask to have the capability to eliminate surface bacteria upon laser irradiation between wearing. Our findings pave the way toward realizing innovative face masks with light-assisted sterilization, high filtration efficiency, preventing cross-contamination, and long-lasting functionalities. The proposed concept could revolutionize next-generation face masks, drastically reducing the waste generated by face masks while improving the performance of conventional surgical masks.

Experimental

Materials

Ethanol (99.5%, Sigma Aldrich), N,N-dimethylformamide (DMF, 99.0%, Sigma Aldrich), hydrochloric acid (HCl, 37.0%, Sigma Aldrich), dimethyl sulfoxide (DMSO, 99.9%, Sigma Aldrich), hexamethyldisilane (HDMS, 99.0% Sigma Aldrich), formaldehyde (36.0%, Sigma Aldrich), glutaraldehyde (GTA, Sigma Aldrich), polyacrylonitrile (PAN, Mw=150 kDa, Sigma Aldrich), sodium chloride fine particles (NaCl, 0.3 µm), phosphate buffered saline (PBS, pH~7.4, Sigma Aldrich), gold nanorods (Au NRs, λ_a = 810 nm, O.D. = 50, Au NR ≈ 1 mg/mL nanoComposix, USA), nonwoven protective face mask (TZMO SA), DMEM/F-12 (Sigma Aldrich), FBS (F9665, Sigma Aldrich), penicillin (Sigma Aldrich), streptomycin (Sigma Aldrich), baby hamster kidney cell (BHK-21, ThermoFisher Scientific), Glascow's MEM (GMEM, ThermoFisher Scientific), tributyl phosphate (TBP, Sigma Aldrich), 4-(2-hydroxyethyl)-1-piperazineethanesulfonic acid (HEPES, ThermoFisher Scientific), *Staphylococcus aureus* (*S. aureus*, ATCC® 6538™, Pol-AURA), tryptic soy agar (TSA, bioMérieux SA, Marcy-l'Etoile, France), 2,4,5-Trimethylthiazole (TMS, 98.0%, Sigma Aldrich), MTS cell

proliferation reagent (BioVision), FM™ 4-64 (Invitrogen, ThermoFisher Scientific), ROTI® Mount FluorCare DAPI (Carl Roth), and Alexa Flour 568 (ThermoFisher Scientific) , lysogeny broth (LB) and lysogeny agar (LB agar, A&A Biotechnology).

Fabrication of nanostructured mask

A 10% w/w solution of PAN in DMF was prepared at room temperature via a magnetic stirrer. Subsequently, the PAN solution was homogenously dissolved overnight and transferred to a 1 mL syringe equipped with a 26-G metal blunt-end needle. A surgical mask was fixed on a stationary collector at a distance of 12 cm from the tip of the needle and connected to the negative pole of the voltage source. The electrospinning conditions were as follows: a flow rate of 500 µL/h and an applied voltage of 12 kV. The environmental conditions of the procedure were kept at a temperature of 24 °C and relative humidity of 44%. To decorate the as-spun PAN nanofibers on the surgical mask via electrospraying, an alcosol suspension of Au NRs was prepared—briefly, 10 µL of 50 O.D. Au NRs were dispersed in a 100 µL water and ethanol solution with a volume ratio of 1:1 and ultrasonicated. An ultrasonic bath was utilized for 15 min to disperse the alcosol for electrospraying. Next, the electrospraying process of Au NRs alcosol was carried out using a 1 mL syringe with a 22-G needle. The electrospraying conditions were as follows: a flow rate of 200 µL/h and an applied voltage of 7 kV at a needle-collector distance of 6 cm. The PAN solution was used again to electrospun the nanostructured face mask's second layer to protect the as-prepared decorated PAN nanofibers. The fabrication and environmental parameters were the same used for the first layer of electrospun PAN fibers.

To calculate the amount of sprayed Au NRs content, we used Equation 1. The following equation, with assuming a continuous flow rate:

$$M = OD \times V \times (Afm / Aes) \quad (1)$$

Where, the optical density of the nanoparticles (OD), Volume of gold nanorods in electrospraying alcosol (V), Afm as the face mask area, and Aes as the electrospraying area. In, the table S4, amount of gold nanorods in each sample has been reported.

Chemical characterizations

To measure the UV-Vis spectra of Au NRs solution from 200 to 1000 nm with a step of 5 nm, a Multiskan GO spectrophotometer (Thermo Scientific, USA) was utilized. The hydrodynamic diameter of Au NRs was measured using a dynamic light scattering (DLS) zeta sizer Nano ZS (Malvern Panalytical, UK).

Morphological studies

The morphological properties of the Au NRs solution used for this study were investigated using the transmission electron microscopy (TEM) method. On the other hand, scanning electron microscopy (SEM) and field-emission electron microscopy (FE-SEM) were carried out to study the morphology of fabricated and decorated nanofibers. SEM investigations were conducted using a JEOL JSM-6390LV microscope. The accelerating voltage was 10 kV at a working distance of 10 mm. TEM, FE-SEM, and Energy-dispersive X-ray spectroscopy (EDAX) were performed using the FEI Nova NanoSEM 450 microscopes. The accelerated voltage for TEM and FE-SEM microscopy was at 10 kV, and for EDAX, the operating voltage was at 15 kV. Before SEM and FE-SEM microscopic imaging, the samples were coated with a 4 nm thick layer of gold using SC7620 Polaron micro sputter coater (Quorum Technologies Ltd., Ashford, UK).

Thermal-activity and antibacterial testing of mask

The Coherent Powerline CW diode laser, which operates at 810 nm in the high absorption range of Au NRs, was used in the thermo-optical setup. Under laser irradiation, the temporal temperature profile and spatial heating distribution were measured and identified using a high-resolution thermal camera (FLIR, A655sc). With an accuracy of 0.2 °C, the camera generates thermal images with a resolution of 640×480 pixels. It smoothly integrates with specialized software (FLIR ResearchIR Max) to capture and process the thermal data that the camera has collected.

Deacetylation and purification of DCFH2

The 2′,7′-dichlorodihydrofluorescein diacetate ($DCFH_2$-DA) deacetylation to 2′,7′-dichlorodihydrofluorescein ($DCFH_2$) and further purification was conducted following the protocol reported by Reiners et al.63 Briefly, the methanol stock solution of $DCFH_2$-DA was neutralized with 0.1 M sodium hydroxide (NaOH). An equal volume of 0.2 M HCl to the NaOH fraction was gradually added to precipitate DCFH2. The precipitated pellet was centrifuged at 2000 × g for 15 min at 4 °C. After the supernatant collection, 4 mL of ice-cold acidified MiliQ water (pH = 1) was added, and the centrifugation preceded by acidified MiliQ addition was repeated two more times. Chloroform was used to extract DCFH2 and remove the aqueous phase. The organic phase was evaporated under a continuous stream of argon gas at room temperature. Pellet was dissolved in methanol up to a concentration of 0.05 M. The stock solution was purged with argon gas and stored at -20 °C. All the steps were performed using a probe covered with aluminum foil to shield the sample from light exposure.

Spectrofluorometric DCFH2 oxidation assay in a cell-free system

Deacetylated and purified DCFH2 was used to determine the oxidant-generating potential of Au NRs on the surface of the face mask in the cell-free environment. The face mask with Au NRs was placed in a 96-well plate and poured with 198 µL PBS (pH = 7.4) and 2 µL of $DCFH_2$ (50 µM final concentration). The oxidizing potential during NIR laser irradiation (3.0 W/cm^2) and in the absence of laser was assessed spectrofluorimetrically (λ_{ex} = 485 nm and λ_{em} = 538 nm). Time points T = 0-2.5 min and T = 15-20 min were performed without laser irradiation, whereas time points T = 2.5-15 min were assessed using continuous laser irradiation.

Bacterial Filtration Efficiency

A six-stage cascade impactor (WES-710, Westech Instrument, Upper Stondon, Great Britain) was implemented to fix the face masks for bacterial filtration efficiency (BFE) tests. Also, an aerosol chamber using a collision nebulizer (MRE CN25, BGI Incorporated, Waltham, MA, USA) was used for the BFE test. The absorbance of cells was measured using a microplate

reader (Tecan Sunrise, Tecan Group Ltd., Männedorf, Switzerland) at the optical density (O.D.) of 490 nm.

Before each experiment, the tested masks were conditioned at 21 ± 0.5 °C and 85 ± 5% relative humidity for a minimum of 4 h to bring them into equilibrium with the atmosphere before testing. BFE was determined for each set of tested masks according to the European Standard EN 14683:2019+AC. Briefly, a tested mask was clamped between an inlet and the first stage of a six-stage cascade impactor (WES-710, Westech Instrument, Upper Stondon, Great Britain). An aerosol of *Staphylococcus aureus* (ATCC 6538) was introduced (from suspension in peptone water) into an aerosol chamber using a Collision nebulizer (MRE CN25, BGI Incorporated, Waltham, MA, USA) and subsequently drawn through the tested mask and the impactor under vacuum loaded with six Petri plates filled with tryptic soy agar (TSA, bioMérieux SA, Marcy-l'Etoile, France). The flow rate through the impactor during testing was equal to 28.3 L/min, and the duration of each test was 2 min. The testing was performed with the inside of the mask in contact with the bacterial challenge aerosol. The tested area of each mask was equal to 52.78 cm^2. For each tested mask, its BFE was given by the number of colony-forming units (CFU) passing through the mask material expressed as a percentage of the CFU present in the challenge aerosol. To calculate BFE, the following Equation 2 was used:

$$BFE = ((C - T)) / (C) \times 100 \quad (2)$$

Where:

C is the mean of the total plate counts for the two positive control runs,

T is the total plate count for the tested mask.

Negative and positive control runs supplemented each test with the mask. A negative control run was performed by passing air, without adding the bacterial challenge, through the cascade impactor for 2 min. Positive control run without a tested mask was done twice, before and after tests using an impactor fully loaded with TSA plates. The first positive control run was carried out at the beginning of the tests. After the last mask was tested, the second positive control run was performed. The duration of each of them was also 2 min.

After each aerosol sampling, the Petri plates were incubated at 37 ± 2 °C for 20 to 52 h. After incubation, the number of bacterial colonies on each impactor plate was counted (considering the 'positive hole' conversion table provided by the impactor manufacturer), and the counts were added to the total number of CFU collected by the impactor.

Filterability and breathability measurements

An automated filter tester provided by Zhaohui Filter Technology Co. Ltd., China, was used to measure filtration efficiency and airflow resistance. The tester could deliver charge-neutralized monodisperse solid NaCl aerosol particles that had a mass mean diameter of 300–500 nm and a geometric standard deviation not exceeding 1.92. The neutralized NaCl aerosol particles were fed into a filter holder and down through the filter with 100 cm^2 of effective area.

Cell study

Confocal microscope LSM710 (Carl Zeiss, Munich, Germany) and Zen software (Zeiss) was used to visualize cells on the mask and verify the MTS assay results. Using the goniometer Data Physics OCA 15EC (Filderstadt, Germany), water contact angle measurements were used to determine the face mask's hydrophobicity.

Cell culture

Baby hamster kidney cells (BHK-21) were grown on a GMEM medium supplemented with 10% FBS, 2% TPB, 10 mL of 1M HEPES, 100 µg/mL penicillin, and 100 µg/mg streptomycin. Cells were maintained at 37 °C in a 5% CO_2 incubator.

Indirect cell viability

Cells were seeded onto a 24-well plate at a density of 50000 cells in a volume of 500 µL medium per well. The pieces of masks with the size of 1.5 × 1.5 cm were cut out and incubated in 1 mL of the cell growth medium. Cells were cultured at 37 °C and 5% CO_2 for 24 h. Then the culture medium of cells was replaced with 0.5 mL of the medium in contact with the mask samples. Untreated cells growing on the bottom of the 24-well plate were used as a control. After 24 h of incubation at 37 °C and 5% CO_2, 50 µL of MTS cell proliferation reagent (Biovision) was added to all the wells. Medium cultured in the absence of cells was used as a background and subtracted from the results. Samples were incubated for 1 h until a color change was visible. 200 µL of samples from the 24-well plate were transferred to the 96-well plate, making technical duplicates for each condition. The absorbance was measured using a microplate recorder (Tecan Sunrise) at the O.D. of 490 nm.

Direct cell viability

Mask samples of 1.5 × 1.5 cm were cut out and put into CellCrown™ 24-well plate inserts. Cells at density 50000 cells in a volume of 500 µL medium were seeded onto each mask sample. An additional 750 µL of the medium was added into the wells and incubated at 37 °C and 5% CO_2. Incubation times were 24 h, 48 h, 72 h, 5days, and 7 days. 500 µL of the medium was replaced with a fresh medium every 48 h. As a control, untreated cells growing at the bottom of the 24-well plate wells were selected. Background conditions were created by adding 1.25 mL of the fresh medium into the empty walls. After incubation, 125 µL of MTS Cell Proliferation reagent was added to the cells, control, and background wells. After 1 h of incubation, the O.D. measurements were performed following the same protocol reported for the indirect method.

Cell morphology

Confocal microscope LSM710 (Carl Zeiss, Munich, Germany) and Zen software (Zeiss) was used to visualize cells on the mask after direct cell viability testing (masks were replaced between CellCrown™ inserts) and confirm the MTS assay results. The only difference was that the cells were seeded onto the mask samples at the density of 100000 cells in 500 µL medium per well and incubated at 37 °C and 5% CO_2 for 48 h. After the incubation, the mask pieces with cells were removed from the inserts and washed with 1× PBS solution, after which they were fixed with 3.7% formaldehyde for 10 min at room temperature. After fixation, mask pieces with cells were washed with 1 x PBS

and permeabilized with 0.1% Triton-X solution for 3 min at room temperature. After permeabilization, the mask pieces were again washed with 1 x PBS. Then the mask pieces with cells were placed on the microscopy slide and stained with 10 µL of the staining solution containing DAPI and Alexa 568 in 1 x PBS. A drop of ROTI®Mount FluorCare DAPI (Carl Roth, Karlsruhe, Germany) was added. The sample was covered with microscopy cover glass and sealed with nail polish. Samples were visualized under the microscope. In addition, microscopy analyses were performed to confirm that the fixation process did not affect the cells on mask staining without fixation (Supportive information, Fig. S8). For this analysis, the same protocol as above was used, but after 48 h of incubation, the samples seeded with cells were removed from the inserts, washed in 1 × PBS solution, and treated with 50 µL of 10 µg/mL FM 4-64 (Invitrogen, ThermoFisher, USA) staining solution in DMSO. After 2 min, the mask pieces were placed on a microscope slide and visualized under the microscope.

Bacterial culture

S. aureus (ATCC 6538) was cultured on lysogeny broth (LB) agar and isolated with a streak plate method. An isolated colony was inoculated in 3 mL of fresh LB broth for a test and grown overnight at 37 °C in an orbital shaker.

NIR-light-activated bacterial inactivation

NIR Inactivation studies were performed in sterile flat-bottom 96-well plates. Briefly, the materials were cut into 6 mm diameter circles, sterilized under UV light on both sides for one hour (30 min per side) to reduce the bioburden, and glued to the bottom of the wells. *S. aureus* bacteria were cultured overnight in LB broth. Afterward, the bacterial culture was adjusted to 5×105 colony-forming units (CFU/mL) by adding fresh PBS. 100 µL of the bacterial solution was added to each well onto the materials' surface. The 96-well plate was subjected to NIR irradiation for 15 minutes upon reaching the target temperature of 60 °C. The pure bacterial suspension was used as a positive control. The test was conducted in triplicate for each material, while non-irradiated control samples were incubated in the dark at room temperature for 20 min. After irradiation or dark incubation, 100 µL of sterile PBS was added to each well to resuspend the bacteria. Then, 100 µL aliquots were transferred to another 96-well plate and serially diluted. Each dilution was plated on LB agar in 3 technical repetitions. The plates were then incubated at 37 °C overnight, and afterward, the bacterial colonies were counted to estimate the bacteria's survival.

The plating technique limited the highest degree of inactivation detectable and amounted to 3 log units of detection in CFU/mL, starting from 5×10^5 CFU/mL, thus allowing for the detection of survival rates ≥0.1%.

Finally, to provide high-quality macroscopic observations and the possibility to detect bacteria at a survival rate as low as 0.05%, each suspension was further diluted 10 more times, and 100 µL of each dilution was spread evenly on LB agar plates (representative plates) and incubated at 37 °C overnight.

Statistical analysis for filtration efficiency

The data on filtration efficiency for each group of tested masks were checked for the normality of their distribution. In the three tested cases (i.e., A, B, and C), the Kolmogorov-Smirnov, Lilliefors, and Shapiro-Wilk's W tests revealed that all analyzed data in each group had a normal distribution. Hence, the analysis of the variance (ANOVA) was carried out to check the differences between groups of tested masks. The ANOVA showed that the BFE for surgical masks significantly differed from BFE for masks fabricated samples (Scheffe tests: in both cases $p<0.000001$). There was no significant statistical difference between BFE calculated for single and double electrospun layer masks ($p>0.05$).

Statistical analysis for cell viability

To calculate live cell population percentages, the following equations were used.

Equation 3:

cell viability (%) = ((sample O.D. - background O.D.)) / ((control O.D. - background O.D.)) × 100 (3)

Equation 4:

cell viability (%) = (sample O.D.) / (control O.D.) × 100 (4)

All experiments were performed once in three replicates. Results are expressed as an arithmetic mean ± SD. Statistical analysis was performed using one-way ANOVA and post hoc pairwise t-tests with MS Excel 365 software ($p < 0.05$). Holm's method was used for adjusting in the case of multiple comparisons.

Author Contributions

F.P. and L.D.S. convinced the idea. F.P., P.N., and M.A.H.B. designed the experiment. M.A.H.B. fabricated the platforms and performed chemical characterization and photothermal characterizations. C.R. and O.C. conducted bacterial studies. D.R. and S.S.Z. Performed the photodynamic experiment. M.A.H.B., A.Z., and P.N. performed the morphological characterization. K.P.P. and K.K. carried out in vitro tests. S.Z. and B.D. Performed particle filtration tests. A.S-K. and R.L.G. carried out the bacterial filtration tests. M.A.H.B. wrote the manuscript. All authors discussed the results and commented on the manuscript. F.P. supervised the project.

Conflicts of interest

There are no conflicts to declare.

Acknowledgments

This work was supported by the National Science Centre (NCN) SONATA BIS Project No. 2020/38/E/ST5/00456. This research was supported by the Estonian Research Council grant PRG1507 (K. Kogermann). Figures 1, 3a, 4a, 5a, 5b, 6a, 7a, and 8a were created with Biorender; Figures 5c, S3, and S5 were partially created with Biorender. C.R., P.N., and F.P. acknowledge the financial support from the Polish Ministry of Science and Higher Education through scholarships for outstanding young scientists.

Notes and references

1 Piscitelli P, Miani A, Setti L, et al (2022) The role of outdoor and indoor air quality in the spread of SARS-CoV-2: Overview and recommendations by the research group on COVID-19 and particulate matter (RESCOP commission). Environ Res 211:113038. https://doi.org/10.1016/J.ENVRES.2022.113038

2 Domingo JL, Rovira J (2020) Effects of air pollutants on the transmission and severity of respiratory viral infections. Environ Res 187:109650. https://doi.org/10.1016/J.ENVRES.2020.109650

3 Lee HR, Liao L, Xiao W, et al (2021) Three-Dimensional Analysis of Particle Distribution on Filter Layers inside N95 Respirators by Deep Learning. Nano Lett 21:651–657. https://doi.org/10.1021/ACS.NANOLETT.0C04230

4 Stadnytskyi V, Anfinrud P, Bax A (2021) Breathing, speaking, coughing or sneezing: What drives transmission of SARS-CoV-2? J Intern Med 290:1010–1027. https://doi.org/10.1111/JOIM.13326

5 Niazi S, Groth R, Spann K, Johnson GR (2021) The role of respiratory droplet physicochemistry in limiting and promoting the airborne transmission of human coronaviruses: A critical review. Environmental Pollution 276:. https://doi.org/10.1016/J.ENVPOL.2020.115767

6 Salian VS, Wright JA, Vedell PT, et al (2021) COVID-19 Transmission, Current Treatment, and Future Therapeutic Strategies. Mol Pharm 18:754–771. https://doi.org/10.1021/ACS.MOLPHARMACEUT.0C00608

7 Cho Y, Son Y, Ahn J, et al (2022) Multifunctional Filter Membranes Based on Self-Assembled Core-Shell Biodegradable Nanofibers for Persistent Electrostatic Filtration through the Triboelectric Effect. ACS Nano 16:19451–19463. https://doi.org/10.1021/ACSNANO.2C09165

8 Xu X, Ha SU, Basnet R (2016) A Review of Epidemiological Research on Adverse Neurological Effects of Exposure to Ambient Air Pollution. Front Public Health 4:157. https://doi.org/10.3389/FPUBH.2016.00157

9 Han S, Kim J, Lee Y, et al (2022) Transparent Air Filters with Active Thermal Sterilization. Nano Lett 22:524–532. https://doi.org/10.1021/ACS.NANOLETT.1C02737

10 Wang X, Xu Z, Su H, et al (2021) Ambient particulate matter (PM1, PM2.5, PM10) and childhood pneumonia: The smaller particle, the greater short-term impact? Science of The Total Environment 772:145509. https://doi.org/10.1016/J.SCITOTENV.2021.145509

11 Zhang S, Liu H, Tang N, et al (2019) Highly Efficient, Transparent, and Multifunctional Air Filters Using Self-Assembled 2D Nanoarchitectured Fibrous Networks. ACS Nano. https://doi.org/10.1021/ACSNANO.9B07293

12 Liu H, Yu J, Zhang S, Ding B (2022) Air-Conditioned Masks Using Nanofibrous Networks for Daytime Radiative Cooling. Nano Lett 22:9485–9492. https://doi.org/10.1021/ACS.NANOLETT.2C03585

13 Kodros JK, O'Dell K, Samet JM, et al (2021) Quantifying the Health Benefits of Face Masks and Respirators to Mitigate Exposure to Severe Air Pollution. Geohealth 5:e2021GH000482. https://doi.org/10.1029/2021GH000482

14 Jin X, Gao F, Qin M, et al (2021) How to Make Personal Protective Equipment Spontaneously and Continuously Antimicrobial (Incorporating Oxidase-like Catalysts). ACS Nano. https://doi.org/10.1021/ACSNANO.1C11647

15 Ullah S, Ullah A, Lee J, et al (2020) Reusability Comparison of Melt-Blown vs Nanofiber Face Mask Filters for Use in the Coronavirus Pandemic. ACS Appl Nano Mater 3:7231–7241. https://doi.org/10.1021/ACSANM.0C01562

16 Iheduru-Anderson K (2021) Reflections on the lived experience of working with limited personal protective equipment during the COVID-19 crisis. Nurs Inq 28:. https://doi.org/10.1111/NIN.12382

17 de Sio L, Ding B, Focsan M, et al (2021) Personalized Reusable Face Masks with Smart Nano-Assisted Destruction of Pathogens for COVID-19: A Visionary Road. Chemistry - A European Journal 27:6112–6130. https://doi.org/10.1002/CHEM.202004875

18 Tuñón-Molina A, Takayama K, Redwan EM, et al (2021) Protective Face Masks: Current Status and Future Trends. ACS Appl Mater Interfaces 13:56725–56751. https://doi.org/10.1021/ACSAMI.1C12227

19 El-Atab N, Qaiser N, Badghaish H, et al (2020) Flexible Nanoporous Template for the Design and Development of Reusable Anti-COVID-19 Hydrophobic Face Masks. ACS Nano 14:7659–7665. https://doi.org/10.1021/ACSNANO.0C03976

20 Ye Z, Ling Y, Yang M, et al (2022) A Breathable, Reusable, and Zero-Power Smart Face Mask for Wireless Cough and Mask-Wearing Monitoring. ACS Nano 16:5874–5884. https://doi.org/10.1021/ACSNANO.1C11041

21 Torres FG, De-la-Torre GE (2021) Face mask waste generation and management during the COVID-19 pandemic: An overview and the Peruvian case. Science of The Total Environment 786:147628. https://doi.org/10.1016/J.SCITOTENV.2021.147628

22 Varghese G, Deepthi PJ, David A, et al (2022) Experimental and Simulation Studies on Nonwoven Polypropylene− Nitrile Rubber Blend: Recycling of Medical Face Masks to an Engineering Product. 7:4791–4803. https://doi.org/10.1021/acsomega.1c04913

23 Sangkham S (2020) Face mask and medical waste disposal during the novel COVID-19 pandemic in Asia. Case Studies in Chemical and Environmental Engineering 2:100052. https://doi.org/10.1016/J.CSCEE.2020.100052

24 Yousefi M, Oskoei V, Jonidi Jafari A, et al (2021) Municipal solid waste management during COVID-19 pandemic: effects and repercussions. Environmental Science and Pollution Research 28:32200–32209. https://doi.org/10.1007/S11356-021-14214-9

25 Xue J, Wu T, Dai Y, Xia Y (2019) Electrospinning and electrospun nanofibers: Methods, materials, and applications. Chem Rev 119:5298–5415. https://doi.org/10.1021/ACS.CHEMREV.8B00593

26 Nakielski P, Pierini F (2019) Blood interactions with nano- and microfibers: Recent advances, challenges and applications in nano- and microfibrous hemostatic agents. Acta Biomater 84:63–76. https://doi.org/10.1016/J.ACTBIO.2018.11.029

27 Ziai Y, Petronella F, Rinoldi C, et al (2022) Chameleon-inspired multifunctional plasmonic nanoplatforms for biosensing applications. NPG Asia Materials 2022 14:1 14:1–17. https://doi.org/10.1038/s41427-022-00365-9

28 M. A. Haghighat Bayan, F. Afshar Taromi, M. Lanzi and F. Pierini, Scientific Reports 2021 11:1, 2021, 11, 1–11. https://doi.org/10.1038/s41598-021-00580-4

29 Huang C, Soenen SJ, Rejman J, et al (2011) Stimuli-responsive electrospun fibers and their applications. Chem Soc Rev 40:2417–2434. https://doi.org/10.1039/C0CS00181C

30 Han D, Yu X, Chai Q, et al (2017) Stimuli-Responsive Self-Immolative Polymer Nanofiber Membranes Formed by Coaxial Electrospinning. ACS Appl Mater Interfaces 9:11858–11865. https://doi.org/10.1021/ACSAMI.6B16501/SUPPL_FILE/AM6B16501_SI_001.PDF

31 Haghighat Bayan MA, Dias YJ, Rinoldi C, et al (2023) Near-infrared light activated core-shell electrospun nanofibers decorated with photoactive plasmonic nanoparticles for on-

demand smart drug delivery applications. Journal of Polymer Science. https://doi.org/10.1002/POL.20220747
32 Zakrzewska A, Haghighat Bayan MA, Nakielski P, et al (2022) Nanotechnology Transition Roadmap toward Multifunctional Stimuli-Responsive Face Masks. ACS Appl Mater Interfaces 14:46123–46144. https://doi.org/10.1021/ACSAMI.2C10335
33 Rinoldi C, Ziai Y, Zargarian SS, et al (2022) In Vivo Chronic Brain Cortex Signal Recording Based on a Soft Conductive Hydrogel Biointerface. ACS Appl Mater Interfaces. https://doi.org/10.1021/ACSAMI.2C17025
34 Annur D, Wang ZK, Liao J der, Kuo C (2015) Plasma-Synthesized Silver Nanoparticles on Electrospun Chitosan Nanofiber Surfaces for Antibacterial Applications. Biomacromolecules 16:3248–3255. https://doi.org/10.1021/ACS.BIOMAC.5B00920
35 Ballesteros CAS, Correa DS, Zucolotto V (2020) Polycaprolactone nanofiber mats decorated with photoresponsive nanogels and silver nanoparticles: Slow release for antibacterial control. Materials Science and Engineering: C 107:110334. https://doi.org/10.1016/J.MSEC.2019.110334
36 Aravind M, Amalanathan M, Aslam S, et al (2023) Hydrothermally synthesized Ag-TiO2 nanofibers (NFs) for photocatalytic dye degradation and antibacterial activity. Chemosphere 321:138077. https://doi.org/10.1016/J.CHEMOSPHERE.2023.138077
37 Mariello M, Qualtieri A, Mele G, De Vittorio M (2021) Metal-Free Multilayer Hybrid PENG Based on Soft Electrospun/-Sprayed Membranes with Cardanol Additive for Harvesting Energy from Surgical Face Masks. ACS Appl Mater Interfaces 13:20606–20621.https://doi.org/10.1021/ACSAMI.1C01740/ https://doi.org/10.1021/ACSAMI.1C01740/SUPPL_FILE/AM1C01740_SI_004.MOV
38 Giljohann DA, Seferos DS, Daniel WL, et al (2010) Gold Nanoparticles for Biology and Medicine. Angewandte Chemie International Edition 49:3280–3294. https://doi.org/10.1002/ANIE.200904359
39 Jeong HH, Choi E, Ellis E, Lee TC (2019) Recent advances in gold nanoparticles for biomedical applications: from hybrid structures to multi-functionality. J Mater Chem B 7:3480–3496. https://doi.org/10.1039/C9TB00557A
40 Kang J, Yeom G, Jang H, et al (2019) Development of Replication Protein A-Conjugated Gold Nanoparticles for Highly Sensitive Detection of Disease Biomarkers. Anal Chem 91:10001–10007. https://doi.org/10.1021/ACS.ANALCHEM.9B01827
41 Wang Q, Ren ZH, Zhao WM, et al (2022) Research advances on surface plasmon resonance biosensors. Nanoscale 14:564–591. https://doi.org/10.1039/D1NR05400G
42 Wang Y, Wang Y, Aravind I, et al (2022) In Situ Investigation of Ultrafast Dynamics of Hot Electron-Driven Photocatalysis in Plasmon-Resonant Grating Structures. J Am Chem Soc 144:3517–3526. https://doi.org/10.1021/JACS.1C12069
43 A. R. Peringath, M. A. H. Bayan, M. Beg, A. Jain, F. Pierini, N. Gadegaard, R. Hogg and L. Manjakkal, J Energy Storage, 2023, 73, 108811. https://doi.org/10.1016/J.EST.2023.108811
44 Guglielmelli A, Pierini F, Tabiryan N, et al (2021) Thermoplasmonics with Gold Nanoparticles: A New Weapon in Modern Optics and Biomedicine. Adv Photonics Res 2:2000198. https://doi.org/10.1002/ADPR.202000198
45 Nakielski P, Pawłowska S, Rinoldi C, et al (2020) Multifunctional Platform Based on Electrospun Nanofibers and Plasmonic Hydrogel: A Smart Nanostructured Pillow for Near-Infrared Light-Driven Biomedical Applications. ACS Appl Mater Interfaces 12:54328–54342. https://doi.org/10.1021/ACSAMI.0C13266
46 Younis MR, An RB, Yin YC, et al (2019) Plasmonic Nanohybrid with High Photothermal Conversion Efficiency for Simultaneously Effective Antibacterial/Anticancer Photothermal Therapy. ACS Appl Bio Mater 2:3942–3953. https://doi.org/10.1021/ACSABM.9B00521
47 Zhong Y, Zheng XT, Zhao S, et al (2022) Stimuli-Activable Metal-Bearing Nanomaterials and Precise On-Demand Antibacterial Strategies. ACS Nano 16:19840–19872. https://doi.org/10.1021/ACSNANO.2C08262
48 P. Li, J. Li, X. Feng, J. Li, Y. Hao, J. Zhang, H. Wang, A. Yin, J. Zhou, X. Ma and B. Wang, Nature Communications 2019 10:1, 2019, 10, 1–10. https://doi.org/10.1038/s41467-019-10218-9
49 P. Kumar, S. Roy, A. Sarkar and A. Jaiswal, ACS Appl Mater Interfaces, 2021, 13, 12912–12927. https://doi.org/10.1021/ACSAMI.1C00083
50 W. Guo, W. Gao, Q. Li, S. Qu, L. Zhang, L. L. Tan and L. Shang, J Mater Chem A Mater, 2023, 11, 2391–2401. https://doi.org/10.1039/D2TA09061A
51 L. Shao, S. Majumder, Z. Liu, K. Xu, R. Dai and S. George, J Photochem Photobiol B, 2022, 231, 112450. https://doi.org/10.1016/J.JPHOTOBIOL.2022.112450
52 Gao S, Yue W, Park CS, et al (2017) Aluminum Plasmonic Metasurface Enabling a Wavelength-Insensitive Phase Gradient for Linearly Polarized Visible Light. ACS Photonics 4:322–328. https://doi.org/10.1021/ACSPHOTONICS.6B00783
53 Lan Z, Lei Y, Chan WKE, et al (2020) Near-infrared and visible light dual-mode organic photodetectors. Sci Adv 6:. https://doi.org/10.1126/SCIADV.AAW8065
54 Yang W, Xia B, Wang L, et al (2021) Shape effects of gold nanoparticles in photothermal cancer therapy. Materials Today Sustainability 13:100078. https://doi.org/10.1016/J.MTSUST.2021.100078
55 Soliwoda K, Rosowski M, Tomaszewska E, et al (2015) Electrospray deposition of gold nanoparticles from aqueous colloids on solid substrates. Colloids Surf A Physicochem Eng Asp 486:211–217. https://doi.org/10.1016/J.COLSURFA.2015.09.035
56 H. Aldewachi, T. Chalati, M. N. Woodroofe, N. Bricklebank, B. Sharrack and P. Gardiner, Nanoscale, 2017, 10, 18–33. https://doi.org/10.1039/C7NR06367A
57 Passaglia E, Campanella B, Coiai S, et al (2021) Agri-Food Extracts Effectiveness in Improving Antibacterial and Antiviral Properties of Face Masks: A Proof-of-Concept Study. ChemistrySelect 6:2288–2297. https://doi.org/10.1002/SLCT.202004678
58 Xiong SW, Fu PG, Zou Q, et al (2021) Heat Conduction and Antibacterial Hexagonal Boron Nitride/Polypropylene Nanocomposite Fibrous Membranes for Face Masks with Long-Time Wearing Performance. ACS Appl Mater Interfaces 13:196–206. https://doi.org/10.1021/ACSAMI.0C17800
59 Chompoosor A, Saha K, Ghosh PS, et al (2010) The Role of Surface Functionality on Acute Cytotoxicity, ROS Generation and DNA Damage by Cationic Gold Nanoparticles. Small 6:2246–2249. https://doi.org/10.1002/SMLL.201000463
60 Higashi Y, Mazumder J, Yoshikawa H, et al (2018) Chemically Regulated ROS Generation from Gold Nanoparticles for Enzyme-Free Electrochemiluminescent Immunosensing. Anal Chem 90:5773–5780. https://doi.org/10.1021/ACS.ANALCHEM.8B00118
61 Nguyen UNT, Do KH, Jang B, et al (2022) Always-on photocatalytic antibacterial facemask with mini UV-LED array. Materials Today Sustainability 18:100117. https://doi.org/10.1016/J.MTSUST.2022.100117
62 Tang P, Zhang Z, El-Moghazy AY, et al (2020) Daylight-Induced Antibacterial and Antiviral Cotton Cloth for Offensive Personal Protection. ACS Appl Mater Interfaces 12:49442–49451. https://doi.org/10.1021/ACSAMI.0C15540
63 Kumar A, Sharma A, Chen Y, et al (2021) Copper@ZIF-8 Core-Shell Nanowires for Reusable Antimicrobial Face Masks. Adv

Funct Mater 31:2008054. https://doi.org/10.1002/ADFM.202008054
64 A. Ray Chowdhuri, S. Tripathy, S. Chandra, S. Roy and S. K. Sahu, RSC Adv, 2015, 5, 49420–49428. https://doi.org/10.1039/C5RA05393E
65 Xiaotong Chen, Tao Yu, Qunshou Kong, et al (2023) A chlorogenic acid functional strategy of anti-inflammation, anti-coagulation and promoted endothelial proliferation for bioprosthetic artificial heart valves. J Mater Chem B 11:2663–2673. https://doi.org/10.1039/D2TB02407A
66 Scungio M, Parlani G (2023) Determining the filtration effectiveness of non-standard respiratory protective devices by an ad-hoc laboratory methodology. Atmos Environ 302:119731. https://doi.org/10.1016/J.ATMOSENV.2023.119731
67 Sipkens TA, Corbin JC, Oldershaw A, Smallwood GJ (2022) Particle filtration efficiency measured using sodium chloride and polystyrene latex sphere test methods. Scientific Data 2022 9:1 9:1–7. https://doi.org/10.1038/s41597-022-01860-y
68 Tong SYC, Davis JS, Eichenberger E, et al (2015) *Staphylococcus aureus* infections: Epidemiology, pathophysiology, clinical manifestations, and management. Clin Microbiol Rev 28:603–661. https://doi.org/10.1128/CMR.00134-14
69 Okkeh M, Bloise N, Restivo E, et al (2021) Gold Nanoparticles: Can They Be the Next Magic Bullet for Multidrug-Resistant Bacteria? Nanomaterials 2021, Vol 11, Page 312 11:312. https://doi.org/10.3390/NANO11020312
70 Seifer S, Elbaum M (2021) Thermal inactivation scaling applied for SARS-CoV-2. Biophys J 120:1054–1059. https://doi.org/10.1016/J.BPJ.2020.11.2259
71 Reiniers MJ, Van Golen RF, Bonnet S, et al (2017) Preparation and Practical Applications of 2',7'-Dichlorodihydrofluorescein in Redox Assays. Anal Chem 89:3853–3857. https://doi.org/10.1021/ACS.ANALCHEM.7B00043